ATLAS NOTE

ATLAS-CONF-2011-043

March 18, 2011

Measurement of multi-jet cross-sections in proton-proton collisions at 7 TeV center-of-mass energy

The ATLAS collaboration

Abstract

Inclusive multi-jet production is studied using the ATLAS detector for proton-proton collisions with a center-of-mass energy of 7 TeV. The data sample corresponds to an integrated luminosity of 2.43 pb^{-1}, using the first proton-proton data collected by the ATLAS detector in 2010. Results on multi-jet cross sections and angular distributions are presented and compared to both leading-order plus parton-shower Monte Carlo predictions and next-to-leading-order QCD calculations.

1 Introduction

At hadron colliders, events containing multiple jets in the final state are prolific and provide a fertile testing ground for the theory of the strong interaction, quantum chromodynamics (QCD). At high transverse momentum (high p_{T}), the production of jets is modeled by QCD as the hard scattering of partons and the subsequent parton showering, followed by a hadronization process. Within the framework of QCD, the jet energy and direction are related to the energy and direction of partons produced in the hadron collisions. Consequentially, the study of energy and angular distributions of multi-jet events provides one of the most fundamental and direct tests of QCD at hadron colliders. The study of multi-jet events in hadron colliders must also contend with additional non-perturbative effects, such as those originating from the underlying event [1].

The study of multi-jet events has, in addition, great relevance to searches for new particles and new interactions at high energies. Events with multiple jets in the final state will often populate searches for high mass particles, and therefore systematic uncertainties that limit the understanding of multi-jet events may carry over into analyses in which multi-jet events represent a significant background.

In this paper, a first study is performed of multi-jet events from proton-proton collisions at 7 TeV center-of-mass energy, using the ATLAS detector at the Large Hadron Collider (LHC) at CERN. The data sample used for the analysis was collected between March 30 and August 29 of 2010 and represents a total integrated luminosity of 2.43 pb^{-1}. With this data sample, after selection cuts, the analysis contains approximately half a million events with at least two jets in the final state.

Results on the total cross section for multi-jet events as a function of the jet multiplicity as well as the differential cross section as a function of the jet p_{T} and the total transverse energy of selected jets in the event, H_{T}, are presented and compared to predictions from leading-order (LO) matrix-element (ME) calculations combined with the parton-shower (PS) approximation for the collinear and infrared regions. Similarly, a study of multi-jet cross section ratios is performed, in which many systematic uncertainties cancel. Studies of the angular distributions of three jet events are also compared to leading-order predictions. Studies of the three-jet to two-jet cross section ratio as a function of a characteristic p_{T} of the event are compared to a next-to-leading-order (NLO) perturbative QCD (pQCD) prediction.

In short, the two primary motivations of the multi-jet study in this paper are, first, to evaluate and understand how robust the leading-order theoretical predictions are for representing the high jet multiplicity QCD final states (relevant also as background to high-energy searches) and, second, to compare next-to-leading-order pQCD calculations as a test of pQCD. For the leading-order studies, events with up to six jets in the final state are studied, and for the next-to-leading-order pQCD study, the focus is on three-jet events and their comparison to two-jet events.

The present ATLAS study represents a more in depth study of multi-jet events compared to initial results presented at the summer conferences in 2010 [2], where a lower energy selection of jet events (down to 30 GeV) was used, with correspondingly higher systematic uncertainties.

2 The ATLAS Detector

The ATLAS experiment consists of an approximately 45-meter long, 25-meter diameter cylindrically shaped detector centered on the proton-proton interaction point. A detailed description of the ATLAS experiment can be found elsewhere [3]. High-energy particles produced in collisions initially pass through an inner detector tracking system embedded in a two-Tesla solenoidal magnetic field. The field is confined to a region of diameter 2.3 meters and 7 meters long also centered at the interaction point. The design of this tracking system allows for measuring charged particle kinematics within the pseudorapid-

ity[1] range of $|\eta| < 2.5$. Precision tracking using the ATLAS pixel detector with a space point resolution as small as 10 microns by 70 microns (in the beam direction) begins at a radial distance of five cm from the interaction point. The identification of the vertex from which the jet originates, performed with this inner tracker is of primary interest in the study of multi-jet events.

Just outside the inner tracker package is a system of liquid argon and scintillating tile calorimeters used for the measurement of particle energies. A liquid-argon/lead electromagnetic calorimeter covers the pseudo-rapidity range of $|\eta| < 3.2$. This calorimeter is complemented by hadronic calorimeters, built using scintillating tiles and iron for $|\eta| < 1.7$ and liquid argon and copper in the end-cap ($1.5 < |\eta| < 3.2$). Forward calorimeters extend the coverage for ATLAS to $|\eta| < 4.9$. In the calorimeters, particles interact through electromagnetic and hadronic processes, allowing the measurement of the particles' energies and directions. The calorimeters are the primary detectors used to reconstruct the jet energy in this analysis.

Outside the calorimeters is a toroidal magnetic field that extends to the edge of the detector. Additional tracking detectors designed for measuring muon kinematics are placed within this magnetic field. The impact of muons in the analysis presented in this paper is negligible.

The ATLAS trigger system employs three trigger levels, of which only the hardware-based first level trigger is used in this analysis. Events are selected using the calorimeter-based jet trigger. The first level calorimeter-based jet trigger [4] uses coarse detector information to identify areas in the calorimeter where energy deposits above a certain threshold occur. A simplified jet finding algorithm based on a sliding window of size $\Delta\phi \times \Delta\eta = 0.8 \times 0.8$ is used to identify these areas. This algorithm uses coarse calorimeter towers with a granularity of $\Delta\phi \times \Delta\eta = 0.2 \times 0.2$ as inputs.

3 Cross Section Definitions and Kinematics

The anti-k_t algorithm [5, 6] with full four-momentum recombination is used to identify jets. For the leading-order analysis, where studies are performed with up to six jets in the final state, the resolution parameter in the jet reconstruction is fixed to $R = 0.4$ to contend with the limited phase space and to reduce the impact of the underlying-event contribution to the jet energy determination. For the next-to-leading-order analysis, where the study focuses on three-jet events, a resolution parameter of $R = 0.6$ is also used, since the study performed with larger R is less sensitive to theoretical scale uncertainties. The anti-k_t algorithm has been chosen because it can be implemented in the next-to-leading-order pQCD calculation, is infra-red safe to all orders and produces jets with a simple geometrical shape.

Jet measurements are corrected for all experimental effects and refer to the particle-level final state. At the particle level, jets are built using all final-state particles with a laboratory-frame lifetime longer than 10 ps, including muons and neutrinos from hadronic decays. These corrections are described in Section 6. The next-to-leading-order pQCD calculation is not interfaced to a Monte Carlo (MC) simulation with hadronization and other non-perturbative effects. The correction for non-perturbative effects is described in Section 4.

Cross sections are calculated in bins of inclusive jet multiplicity, defined as the number of jets with $p_{\mathrm{T}} \geq 60$ GeV and $|y| \leq 2.8$ found in the event. This ensures that jets lie within the efficiency plateau of the triggers used, as described in Section 5. An event with three reconstructed jets satisfying the kinematic cuts thus falls both in the two-jet and the three-jet inclusive jet multiplicity bin. Inclusive multiplicity bins are used because they are stable in the pQCD fixed-order calculation, unlike exclusive bins. The

[1] ATLAS uses a right-handed coordinate system with its origin at the nominal interaction point (IP) in the centre of the detector and the z-axis along the beam pipe. The x-axis points from the IP to the centre of the LHC ring, and the y axis points upward. Cylindrical coordinates (r, ϕ) are used in the transverse plane, ϕ being the azimuthal angle around the beam pipe. The pseudorapidity is defined in terms of the polar angle θ as $\eta = -\ln\tan(\theta/2)$. The rapidity is defined as $y = 0.5 \times \ln[(E + p_z)/(E - p_z)]$, where E denotes the energy and p_z is the component of the momentum along the beam direction. For massless objects, the rapidity and pseudo-rapidity are equivalent.

leading jet is further required to have $p_{\mathrm{T}} \geq 80$ GeV to stabilize the next-to-leading-order calculation [7].

4 Theoretical Predictions

For the leading-order studies, there are several topics of primary interest, and various leading-order Monte Carlo simulations are chosen in an attempt to enhance the sensitivity to these issues. Of primary importance is the study of non-perturbative effects, such as the underlying event (UE). Despite the high p_{T} chosen for this analysis, the increase in the underlying event at the LHC [8] can still have a non-negligible impact on the jet energy determination, particularly when a large resolution parameter ($R = 0.6$) is used in the jet reconstruction. Equally important is the understanding of the differences between the matrix-element/parton-shower (ME+PS) calculation ($2 \rightarrow n$) and the parton-shower calculation ($2 \rightarrow 2$) alone. These topics are not easily separable, since tuning of some of these effects (such as the underlying event) to data is needed, and the tuning process automatically fixes other inputs of the Monte Carlo simulation (such as the parton density function, the parton-shower model, and the hadronization model). For this reason, and due to the large uncertainties otherwise present in the leading-order calculation, no attempt is made to determine a systematic uncertainty in the theoretical leading-order predictions. Instead, a comparison of different Monte Carlo simulations and currently available tunes is performed in order to investigate general features and trends. The different leading-order predictions are normalized to the measured inclusive two-jet cross section to provide a shape comparison, while the overall normalization factors are given to allow understanding the impact of the different tunes on the overall scale of distributions.

For the leading-order analysis, ALPGEN [9] is used to generate matrix elements with up to six partons in the final state using the leading-order set of proton structure functions (pdf) CTEQ6L1 [10]. A factorization and renormalization scale, Q, that varies from event to event is used in the event generation with ALPGEN

$$Q^2 = \sum p_{\mathrm{T}}^2, \tag{1}$$

where the sum runs over all final state partons. ALPGEN is interfaced to PYTHIA [11, 12] and HERWIG/JIMMY [13–16] to sum leading logarithms to all orders in the parton-shower approximation, and include non-perturbative effects such as hadronization and the underlying event. The ATLAS generator tunes from 2009 (MC09′, which only differs from MC09 in the value PARP(82) which is that of the MC08 tune) [17] and from 2010 (AUET1 [18] and AMBT1 [19]) are used for this purpose and have been described previously. Other tunes are also investigated to understand the impact of the underlying-event and parton-shower tuning in the measurements performed. With comparable underlying-event tunes and ALPGEN parameters, the comparison of ALPGEN+PYTHIA to ALPGEN+HERWIG/JIMMY uncovers differences that may arise from different parton-shower implementations and hadronization models used in PYTHIA and HERWIG/JIMMY. A summary of these tunes can be found in Table 1 alongside all other generators and tunes used in this paper.

The PYTHIA 6.421 [11, 12] event generator is also used to study the limitations of the $2 \rightarrow 2$ calculation. This generator implements a leading-order pQCD matrix-element calculation for $2 \rightarrow 2$ scattering, parton showers, an underlying-event model for multiple-parton interactions and the Lund string model for hadronization. The MRST 2007 modified leading order [21, 22] (CTEQ5L) parton distribution function interfaced with the AMBT1 [17] (Perugia2010 [20]) generator tune is used for the sample generation.

The generated particles are passed through a full simulation of the ATLAS detector and trigger [24] based on GEANT4 [25] to account for detector effects. Additional proton-proton collisions are added to the hard scatter in the simulation process to reproduce realistic LHC running conditions. Events and jets are selected using the same criteria in data and Monte Carlo simulations.

Generator	pdf	tune	purpose
ALPGEN+HERWIG/JIMMY	CTEQ6L1 [10]	AUET1 [18]	central value*
ALPGEN+HERWIG/JIMMY	CTEQ6L1 [10]	MC09 [17]	UE studies*
ALPGEN+PYTHIA	CTEQ6L1 [10]	MC09′ [17]	PS studies
ALPGEN+PYTHIA	CTEQ6L1 [10]	D6	UE/PS studies
ALPGEN+PYTHIA	CTEQ6L1 [10]	Perugia 6 [20]	UE/PS studies
PYTHIA	MRST2007 LOmod [21, 22]	AMBT1 [19]	UE/PS studies*
PYTHIA	CTEQ5L [23]	Perugia2010 [20]	UE/PS studies

Table 1: Different Monte Carlo generators and tunes used for the leading-order analysis in this paper. The asterisk indicates the samples used to determine the uncertainties on the non-perturbative correction to the next-to-leading-order calculation.

For the next-to-leading-order analysis, the calculation implemented in NLOJet++ [26] is used. The renormalization/factorization scale is given by Equation 1 scaled by a factor κ^2 and with the sum running over final-state jets. κ is 1 for the calculation of the central value. This scale has been shown to provide predictions that are stable against scale variations. The scale uncertainty is calculated using the following set of values of κ: (1,2), (2,1), (0.5,1), (1,0.5), (2,2), (0.5,0.5), with the first value being applied to the renormalization scale calculation and the other to the factorization scale calculation. The envelope of the results obtained with these values is used as the scale systematic uncertainty in the theoretical calculation, while the central value is calculated with $\kappa = 1$ for both scales. Two next-to-leading-order pdf sets have been used in the calculation of the central value of the observables studied and the theoretical uncertainties associated to the pdfs: CTEQ 6.6 [27] and MSTW 2008 nlo [28]. The 90% confidence-limit error sets are used in the evaluation of the pdf uncertainties. The uncertainty on the measurement due to the value of α_S is calculated varying the value of α_S used in each pdf set by ± 0.002.

The NLOJet++ program is a matrix element calculation, and therefore it lacks a parton-shower interface and does not account for non-perturbative effects. To compare to particle-level jet cross sections, supplementary calculations are required. PYTHIA and ALPGEN interfaced to HERWIG/JIMMY are used to generate samples without underlying event. Jets in these samples are reconstructed from partons after the parton shower, and observables are compared at the particle-level in the standard ALPGEN+HERWIG/JIMMY and PYTHIA samples. A multiplicative correction is calculated using the ALPGEN+HERWIG/JIMMY sample,

$$C_{\text{non-pert}} = \frac{o_{\text{UE}}^{\text{particle}}}{o_{\text{no UE}}^{\text{parton}}}, \tag{2}$$

where o is the observable of interest calculated at the particle or parton level in the samples with and without underlying event. The correction factor takes the next-to-leading-order calculation to the particle level. This correction is calculated in three different samples (marked with an asterisk in Table 1). The correction obtained using the ALPGEN+HERWIG/JIMMY AUET1 sample is taken as the default value for the analysis, and the systematic uncertainty is estimated from the maximum spread compared to the results from the other investigated models. The size of this correction is less than 5% in all observables studied at next-to-leading order. The final uncertainty quoted on the next-to-leading-order calculation comes from the quadrature sum of the scale uncertainty, the pdf uncertainty, the uncertainty on α_S and the non-perturbative correction uncertainty.

5 Event Selection and Reconstruction

5.1 Trigger Selection

A set of ATLAS first level (level-1) multi-jet triggers is used to select events for the analysis. Multi-jet triggers require several jets reconstructed with the level-1 sliding window algorithm. Only symmetric (i.e. all jets sharing the same threshold) two-jet and three-jet triggers are needed for this analysis, since the three-jet trigger operated without pre-scaling for the entirety of the data collection period used in this note. The triggers with a 10 GeV level-1 threshold have been shown to be fully efficient for events with two and trhee anti-k_t jets with $R = 0.4$ and $p_{\mathrm{T}} \geq 60$ GeV [29] using events triggered with the minimum bias triggers.

In this analysis, the efficiency for triggering on the leading jet is calculated using the minimum bias triggers. Then, the efficiency of the trigger to fire on the second leading jet is calculated by requiring that the leading jet passes the single-jet trigger, and so on. Figure 1 shows the efficiency for the third leading jet to fire the three-jet trigger as a function of the reconstructed jet p_{T} for jets of $R = 0.4$ (a) and $R = 0.6$ (b). The efficiencies calculated in data are compared to the efficiency from the Monte Carlo detector simulation. The efficiency as a function of jet rapidity is also shown for $R = 0.4$ jets (c) on the plateau ($p_{\mathrm{T}} > 60$ GeV), revealing a small inefficiency in the data that is not present in the Monte Carlo simulation. The event-level efficiency as a function of the closest distance between two selected $R = 0.4$ offline jets for events selected using the three-jet trigger is also shown (d), to help probe possible topological dependences in the trigger. A dependence is observed, as expected by the size of the level-1 jet trigger objects, and the dependence is well described by the Monte Carlo simulation. The efficiency in data for (d) is calculated using events for which the two-jet trigger passed and the two leading jets were associated to level-1 jet objects, assuming that any topological inefficiency will only affect one of the level-1 jet objects. A good agreement between Monte Carlo simulation and data is observed. The three-jet trigger result indicates an inefficiency for events where two jets are near-by. This inefficiency appears to depend weakly on the jet p_{T} and is well described in the detector simulation for events in which the closest distance between selected jets is above 0.45. Since the detector simulation largely accounts for the inefficiency, it is corrected for with other detector effects, as described in Section 6.

Events in the analysis falling in the three-jet inclusive multiplicity bin or higher are selected using the three-jet trigger with a jet threshold of 10 GeV on the level-1 jet objects. Due to large pre-scaling, a combination of several two-jet triggers is used to select events falling in the two-jet *inclusive* multiplicity bin (i.e. three-jet events that do not pass the two-jet triggers because of trigger pre-scales are not used to measure any two-jet cross section). Symmetric two-jet triggers with 10, 15 and 30 GeV are used to maximize the available statistics. In the two-jet bin, triggers are combined exclusively (events in a specific region of phase space are only selected using one trigger) according to the second leading jet p_{T} (required to be 60-80, 80-110 and at least 110 GeV, respectively) and weighted by the luminosity associated to each trigger.

5.2 Vertex Reconstruction

The event vertex or vertices are found using tracks that originate in the beam collision spot [30], satisfy quality criteria [31] and have a transverse momentum above 150 MeV. A vertex is seeded by searching for the global maximum in the distribution of z coordinates of reconstructed tracks. The vertex is fit using the position of this seed along with neighboring tracks. Tracks incompatible with the reconstructed vertex are used to seed new vertices until no tracks are left. This analysis only uses events in which at least one primary vertex with at least five associated tracks has been reconstructed. No cut on the primary vertex position is applied. The *event* vertex (i.e. that from which jets are considered to originate) is defined as the vertex in the event for which the sum of the p_{T} of the tracks associated to that vertex is largest.

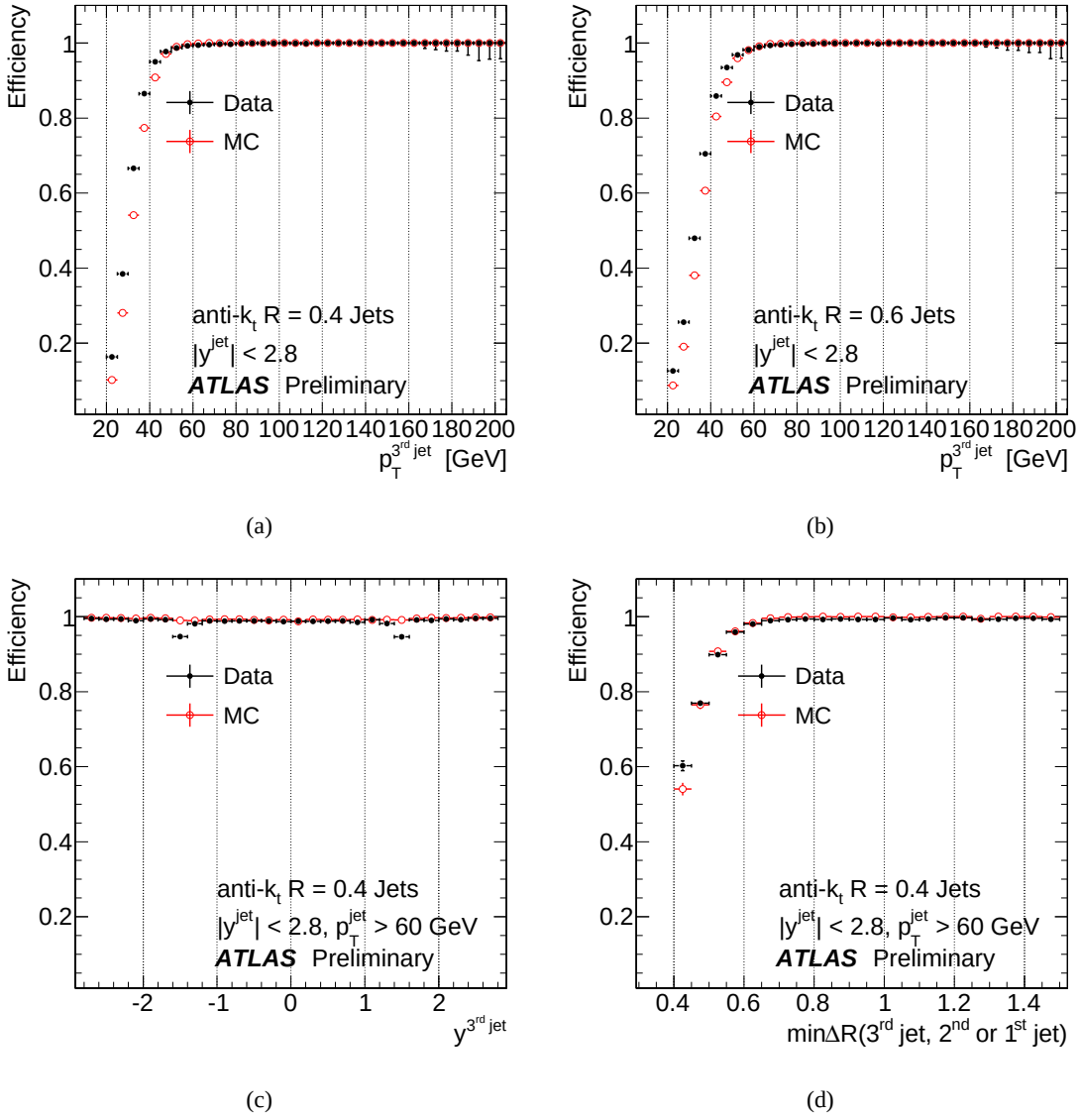

Figure 1: Jet trigger efficiency for the third leading jet as a function of p_{T} for anti-k_t jets with $R = 0.4$ (a), and $R = 0.6$ (b). Jet trigger efficiency as a function of y of the third leading jet with $p_{\mathrm{T}} > 60$ GeV and $R = 0.4$ (c). A topological dependence is found in the efficiency on the plateau ($p_{\mathrm{T}} > 60$ GeV) as a function of the distance between the two closest jets in the event (d) when using jets with $R = 0.4$. The efficiency is shown both as calculated in data with an unbiased method described in the text and in Monte Carlo simulations for the three-jet trigger with a level-1 cut on the transverse energy of the jet of 10 GeV.

5.3 Jet Reconstruction

Topological calorimeter clusters evaluated at the electromagnetic scale [32] are used as inputs to the jet finding algorithm. These clusters use the baseline calibration derived from test beams and from $Z \rightarrow ee$ data [33], which reconstructs the energy of particles interacting electromagnetically. The anti-k_t algorithm [5] with distance parameters $R = 0.4$ and $R = 0.6$ and full four-momentum recombination is used to reconstruct jets from clusters. The jet reconstruction is fully efficient in the Monte Carlo simulation for jets with transverse momentum above 30 GeV. The ATLAS Monte Carlo simulation compares well with the jet reconstruction efficiency measured with data [34].

5.4 Jet Energy Scale Calibration

Jets reconstructed at the electromagnetic scale are measured to have an energy which is lower than the true energy of interacting particles within the jet. This is caused by the different response of the calorimeter to hadrons and electrons and by energy lost in dead material, deposited outside the jet cone or not collected by the cell clustering algorithm. A Monte Carlo-based calibration that corrects for these effects as a function of p_{T} and η is used to obtain jets with the correct energy scale [35]. The jet 4-momentum is calculated assuming that the jet origin is at the position of the event vertex.

5.5 Jet Selection Criteria

Jets considered in the analysis are selected using the following kinematic and data quality selection criteria:

1. An event must contain at least one jet with $|y| \leq 2.8$ and a p_{T} greater than or equal to 80 GeV.
2. Jets are required to have $|y| \leq 2.8$ and $p_{\mathrm{T}} \geq 60$ GeV in order to be counted.
3. A series of jet cleaning cuts were applied to eliminate various detector effects and suppress beam and other non-collision backgrounds. Overall, these cuts reduce the available statistics by less than 0.1%. These cuts have been shown to be efficient in eliminating spurious jets, while rejecting only a negligible number of true jets.
4. Jets are only accepted if at least 70% of their charged particle p_{T} comes from the event vertex (jet vertex fraction, JVF$\geq$ 0.7). Jets with no associated tracks are assigned a jet vertex fraction of -1 and accepted (so the final cut is $|\mathrm{JVF}| \geq 0.7$). Overall, this cut changes the two-jet cross section by 0.4%, and the change increases with multiplicity, reaching 3.4% for the six-jet cross section. The selection has been optimized to minimize the dependence on the number of primary vertices reconstructed for each observable. All observables show a negligible dependence on the number of reconstructed primary vertices when this cut is applied. The results are illustrated, for the inclusive jet multiplicity, in Figure 2.
5. Only events with a minimum of two selected jets are used in the analysis.

For illustrative purposes, Figure 3 presents an event display of a six-jet event passing all selection cuts. The transverse energy deposition in the calorimeter is shown as a function of η and ϕ. For this event, the six selected jets are well separated spatially.

For a total integrated luminosity of 2.43 pb^{-1}, approximately 500,000 multi-jet events survived the selection cuts. Table 2 presents the total number of multi-jet events versus inclusive jet multiplicity. No correction for pre-scales in the two-jet bin has been applied to the numbers in this table.

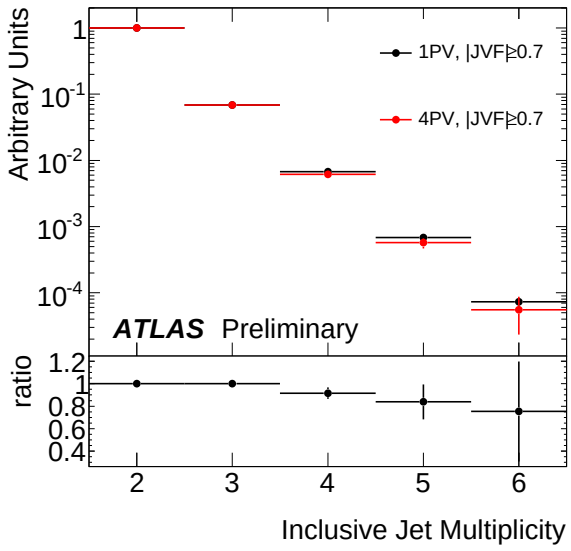

Figure 2: The inclusive jet multiplicity distribution for events containing 1 and 4 primary vertices (PV) after the JVF cut. The distributions are normalized to the first bin. The ratio of the two distributions is shown in the bottom plot.

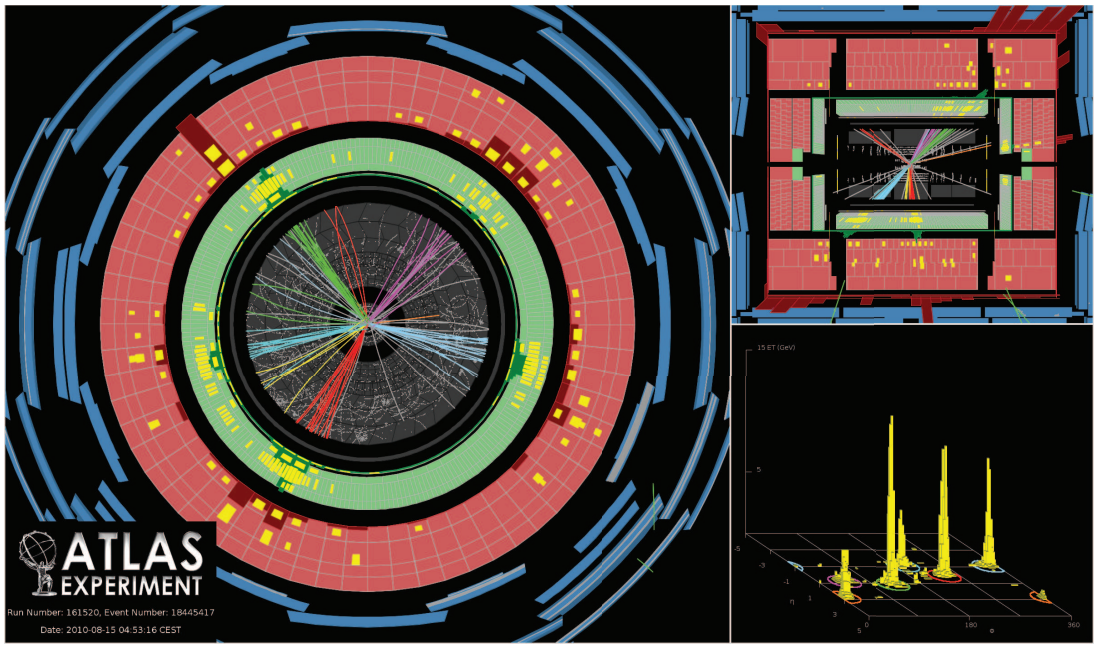

Figure 3: Event display of a six-jet event satisfying the analysis requirements. The towers in the bottom right figure represent transverse energy deposited in the calorimeter projected on a grid of η and ϕ.

Inclusive multiplicity	Number of events
≥ 2	498,157
≥ 3	112,213
≥ 4	10,940
≥ 5	1093
≥ 6	115

Table 2: Number of selected events using the criteria described in this analysis as a function of inclusive jet multiplicity (for anti-k_t $R = 0.4$ jets) before correcting for pre-scales. Events are selected if they have a leading jet $p_{\mathrm{T}} \geq 80$ GeV. Additional jets are counted for that event, if they have $p_{\mathrm{T}} \geq 60$ GeV.

6 Unfolding of Detector Effects

A correction is needed to compare the measurements to theoretical predictions. This correction is applied to the measured distributions so that theoretical comparisons are possible beyond the scope of this note. The correction, which accounts for trigger inefficiencies, detector resolutions and other detector effects that affect the jet counting, is performed in a single step using a bin-by-bin unfolding method by means of a set of Monte Carlo simulations. For each measured distribution, the corresponding Monte Carlo simulation cross section using truth jets as defined in Section 3 is evaluated in the relevant bins, along with the equivalent distributions obtained after the application of detector simulation and analysis cuts. The ratio of the true to the simulated distributions provides the multiplicative correction factor (unfolding factor) to be applied to the measured distributions.

To perform the unfolding, ALPGEN+HERWIG/JIMMY AUET1 Monte Carlo simulation is used. The sample includes, on average, two additional soft proton-proton collision events overlapping with the hard scatter simulated by ALPGEN. The data has fewer overlapping collisions, as revealed by the distribution of the number of selected vertices, and the Monte Carlo simulation is subsequently weighted to match the distribution from the data. The truth distribution is independent of the additional collisions, since jets are built using particles simulated by the ALPGEN+HERWIG/JIMMY Monte Carlo simulation only.

The unfolding uncertainty is estimated taking into account several significant effects. One arises from the spread in correction factors coming from different generators (ALPGEN+ HERWIG/JIMMY AUET1 and PYTHIA AMBT1). Second, a detailed study is performed in which the simulated jet p_{T}, η and ϕ resolution is varied. Third, the shape of the simulated distributions is varied in order to account for possible biases caused by the input distribution. Samples with a trigger inefficiency in the crack region, different JVF cuts (0.5 and 0.9) and different primary vertex distributions are also used to estimate the uncertainty arising from this trigger effect and the impact of overlapping proton-proton collisions. All these effects impact the unfolding systematics, and their uncertainties are ultimately added in quadrature to provide the final systematic uncertainty in the unfolding correction. Statistical uncertainties in the unfolding factors are important for certain bins (particularly for angular measurements), and are added as an independent additional systematic effect. All these effects are described in detail below.

ALPGEN/PYTHIA Differences.

The term that is calculated using the differences between ALPGEN and PYTHIA is the most subtle one, since it combines differences in the jet shapes and parton-shower evolution, which can affect the probability for two jets to be seen as one in the calorimeter, differences in the impact of the additional proton-proton interactions and differences in how the underlying event affects the signal jets. These different effects have been studied individually using samples without additional proton-proton interactions

and this study confirms that no large cancellation of effects between them happens to artificially reduce the systematic uncertainty in the unfolding.

Resolution Smearing.

The term calculated smearing the resolution of the reconstruction of the jet kinematics simply accounts for the limited knowledge of the jet p_{T}, η and ϕ resolution which have been measured in data to within less than 10% [34, 36].

Variation of Shape of Input Distributions.

The term calculated varying the shape of the input distributions accounts for a bias inherent to the bin-by-bin correction. However, since the shape of the distribution is well constrained by our measurement, the shape change used is small, and consistent with shape changes allowed by the systematic uncertainties in the measurement.

Other effects.

The last few terms considered account for the differences between Monte Carlo simulation and data in the trigger efficiencies (see Section 5.1), for the different impact of our JVF cut on the different observables, and for the fact that the vertex distributions are different for events collected with different triggers.

Results on the unfolding factors are presented in Figure 4. The corresponding uncertainties are calculated for the cross section (a) and for the n to $n-1$ cross section ratios (b) as a function of the inclusive jet multiplicity. The combined systematic uncertainty is shown as an orange band around the unfolding

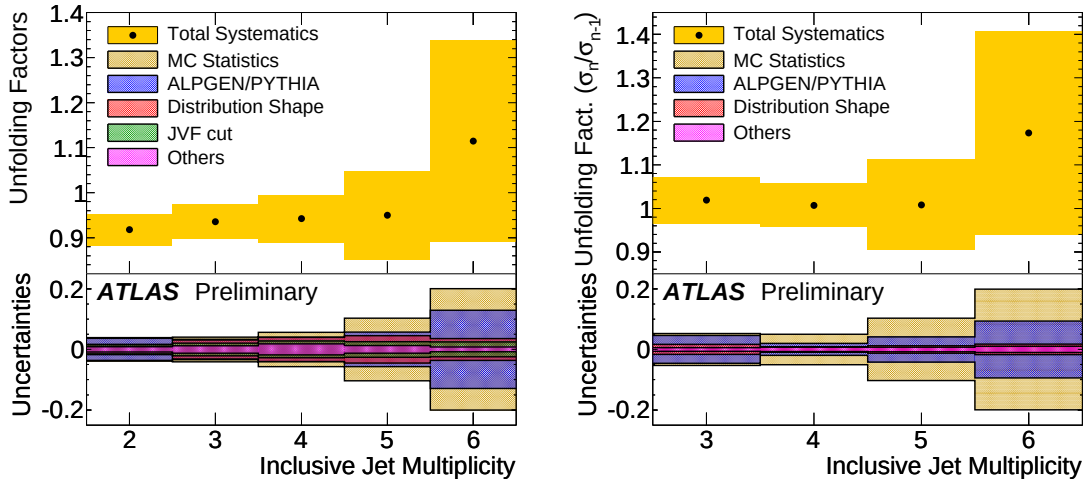

(a) (b)

Figure 4: Unfolding factors for the cross sections (a) and for the n to $n-1$ cross section ratios (b) as a function of the inclusive jet multiplicity. The unfolding factors for the ALPGEN+HERWIG/JIMMY AUET1 sample are shown with the systematic uncertainty as an orange band around the points. See the text for an explanation of the legend labels.

factors. The main components contributing to the systematic uncertainty are shown at the bottom of each figure with different color fills. Although non-negligible, the uncertainty is still smaller than the uncertainty coming from the jet energy scale calibration discussed in the next section for most bins and observables.

7 Systematic Uncertainties

This section focuses on the other systematic effects and uncertainties not discussed yet: the jet energy scale and the luminosity.

The uncertainty in the jet energy scale is the dominant systematic uncertainty for many of the measurements performed in this paper. The rather steeply falling cross sections as a function of jet p_{T} implies that even a relatively small uncertainty in the determination of the jet p_{T} translates into a substantial change in the cross sections as events migrate up or down the steeply falling curve.

The standard jet energy scale uncertainty in ATLAS [35] has been calculated using jets from a dijet sample without near-by activity in the calorimeter. For a multi-jet analysis, a set of additional systematic uncertainties appears that must be addressed. The uncertainties arise from the different calorimeter response to jets of different flavors as well as effects that are sensitive to the available phase space for multi-jet events. These different effects are described below.

7.1 Systematic Uncertainties due to Differences in Light-quark/Gluon Jet Response

Figure 5 shows the calorimeter p_{T} response for light-quark and gluon jets in the barrel as a function

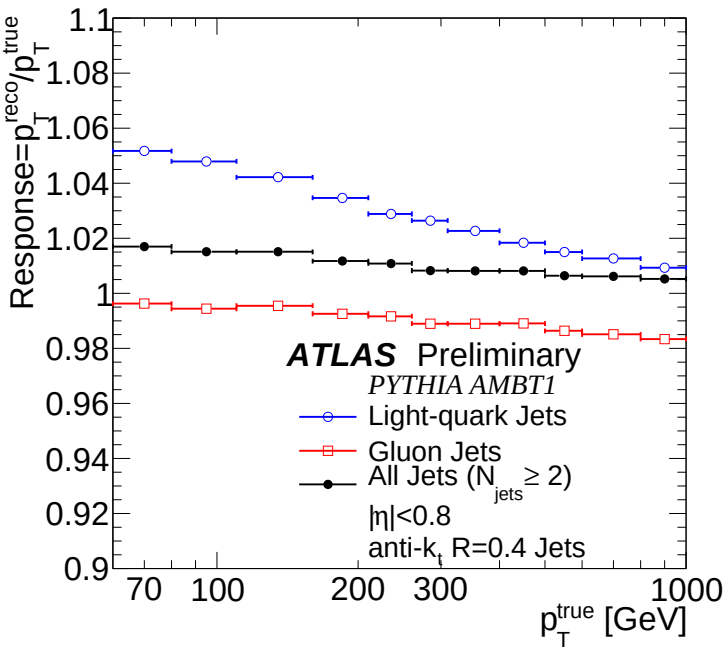

Figure 5: Jet response (mean reconstructed jet p_{T} over true jet p_{T}) as a function of the true p_{T} for jets tagged as originating from a light quark or a gluon. The jet response in a sample with two jets of $p_{\mathrm{T}} \geq 60$ GeV (and with those two jets within $|y| \leq 2.8$) is also shown. The anti-k_t $R = 0.4$ algorithm is used.

of reconstructed jet p_{T} as calculated using the PYTHIA AMBT1 Monte Carlo simulation sample. The response for jets in the two-jet inclusive multiplicity bin is also shown. Light-quark and gluon jets were tagged using the highest-energy parton found in the Monte Carlo simulation particle record within a cone of radius equal to the resolution parameter of the jet algorithm. Only jets that had no other reconstructed jet of uncalibrated $p_{\mathrm{T}} > 7$ GeV within $\Delta R = \sqrt{\Delta\phi^2 + \Delta\eta^2} = 1.0$ from the jet axis were used to decouple flavor composition from topological effects on the response. The Monte Carlo simulation shows slightly

more gluon-like jets for high-multiplicity final states, particularly in the ALPGEN samples.

To the extent that the Monte Carlo simulation reflects the data, the difference in response as a function of multiplicity is accounted for in the unfolding correction. However, additional uncertainties need to be considered because the systematic uncertainty on the jet energy scale was derived for an admixture of light-quark and gluon jets, and for a different admixture it could be different. In addition, the knowledge of the fraction of light-quark and gluon jets in any final state is not perfect.

The first effect has been considered using different Monte Carlo simulations as in Ref. [35] to look at the difference between the gluon and light-quark jet response under different assumptions. In order not to consider twice the effects already included in the jet energy scale systematic derived for the inclusive sample, the gluon and light-quark jet responses have been normalized to the average response of each sample studied. The relative light-quark and gluon jet response is the same within statistical uncertainties under the different assumptions, thus this effect does not contribute to the final jet energy scale systematic uncertainty. The second effect is harder to address, since the effects that impact the details of the admixture (parton distribution functions, limitations of leading-order calculation, initial and final state radiation tuning) are not easy to study consistently. This effect has been treated in a data-driven way using template fits to determine the flavor composition of the sample up to the four-jet inclusive multiplicity bin. The template distributions used were those of the jet width (defined as the p_{T}-weighted average ΔR between the constituents of the jet and the jet axis) and the number of tracks associated to the jet. In these bins, the combination of the two effects impacts the jet energy scale uncertainty by less than 1%.

In the higher multiplicity bins, no specific studies have been performed to constrain the Monte Carlo simulation prediction of the flavor composition of the sample, thus the flavor composition is assumed to be unknown, increasing the overall jet energy scale systematic by up to 3%.

7.2 Systematic Uncertainties due to Jets with Near-by Calorimeter Activity

Jets that have near-by activity require specific studies due to their unique properties, that can impact both the jet energy scale, as well as the size of multiplicity-bin migrations. Their impact in the analysis increases with jet multiplicity, since the probability of a jet having another jet near-by rises as the available phase space (in $[\eta, \phi]$) is used up. Figure 6 shows the probability of a selected jet occurring next to (within $\Delta R = 1.0$) a reconstructed jet of uncalibrated jet $p_{\mathrm{T}} > 7$ GeV as a function of inclusive jet multiplicity. The probability increases with jet multiplicity, and the ALPGEN+HERWIG/JIMMY AUET1 simulation agrees best with data. Differences of up to 10% are observed in PYTHIA AMBT1. These differences affect the rate at which one true jet is reconstructed as two jets in the calorimeter. Since this impacts the size of the detector unfolding corrections, the differences between the different Monte Carlo simulations were used as one component of the detector unfolding systematic uncertainties (see Section 6).

Jets with other near-by jets also have a different jet energy scale, as demonstrated in Monte Carlo simulations. The systematic uncertainty on their energy scale has been evaluated using the balance between two jets (one with near-by calorimeter energy deposits) and the correlation between the p_{T} of the tracks associated to the jet and the p_{T} measured in the calorimeter. The evaluated uncertainty is added in quadrature to the jet energy scale uncertainty calculated for isolated jets in an inclusive sample, increasing the uncertainty on the energy determination for jets with near-by reconstructed jets by at most 1.5% .

7.3 Systematic Uncertainties due to overlapping proton-proton Interactions

Approximately 40% of the selected events have more than one vertex in the interaction, indicating the presence of an additional proton-proton interaction overlapping the event of interest. The vertex multi-

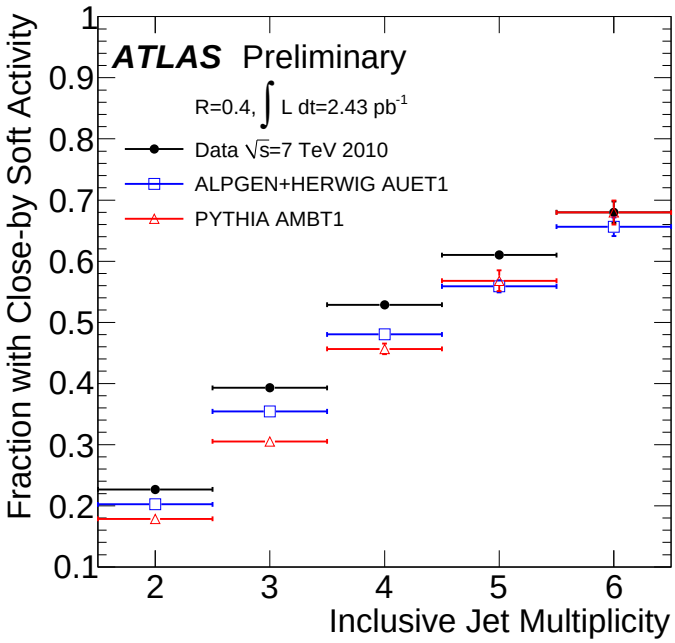

Figure 6: Fraction of selected jets in each inclusive multiplicity bin with neighboring jets within $\Delta R = 1.0$. Data (solid circles) are compared to ALPGEN+HERWIG/JIMMY AUET1 (open squares) and PYTHIA AMBT1 (open triangles).

plicity is low enough that, with a luminous region of several mm and a vertex reconstruction resolution of a few tens of μm, the impact of merged vertices on the analysis is negligible. For the instantaneous luminosities considered in this paper, the probability that two hard events would occur at the same time is negligible. However, a soft interaction occurring in parallel with the hard interaction can produce a contamination of energy from a soft jet in a hard event with which it overlaps.

The average effect of these overlapping interactions on the jet energy scale is accounted for by the offset correction and the systematic uncertainty on that correction has been evaluated [37]. The overlapping interactions can also impact the jet counting by boosting significantly the energy of a soft jet from the hard interaction with the addition of energy from a soft jet coming from the soft interaction. This effect is controlled performing a selection cut on the JVF of the jet as described in Section 5, and an uncertainty due to the efficiency of the cut has been estimated in Section 6.

7.4 Systematic Uncertainties in the Luminosity

The systematic uncertainties in the luminosity calculation affect all cross section measurements, but cancel out in all measurements where cross section ratios are involved. The luminosity of the dataset used in this paper has been calculated to be 2.43±0.08 pb^{-1} [38] and the associated uncertainty is not shown in the figures.

8 Results

In this section, measurements corrected to the particle-level are compared to theoretical predictions. For comparisons to leading-order Monte Carlo simulations, the anti-k_t $R = 0.4$ algorithm is used to define a jet. In Figures 7-14, the orange error band bracketing the measured cross section corresponds to the total

systematic uncertainty, evaluated by adding the individual systematic uncertainties in quadrature except that on the luminosity. The ratio of the Monte Carlo simulation prediction to the data is shown at the bottom of each figure. The leading-order Monte Carlo simulation predictions are normalized to the measured inclusive two-jet cross section, since, as discussed in Section 4, theoretical systematics on these predictions are large, and shape comparisons are thus most relevant. For clarity, only a few representative of all the Monte Carlo simulations studied are shown. The normalization for all the Monte Carlo simulations studied is shown in Table 3, and distinctive features of some of the Monte Carlo simulations not shown are discussed when relevant. Most ALPGEN Monte Carlo simulations used predict an inclusive multi-jet

Leading-order Monte Carlo	Normalization factor
ALPGEN+HERWIG AUET1	1.11
ALPGEN+HERWIG MC09	1.12
ALPGEN+PYTHIA MC09′	1.22
ALPGEN+PYTHIA Perugia6	1.15
ALPGEN+PYTHIA D6	1.62
PYTHIA AMBT1	0.65
PYTHIA Perugia2010	0.84

Table 3: Normalization applied to each of the Monte Carlo simulations used to match the measured two-jet inclusive cross section.

cross section similar to the measured cross section (except for the ALPGEN+PYTHIA D6 tune), while the PYTHIA Monte Carlo simulations require large scaling factors to describe the inclusive multiplicity spectrum. The differences in the normalization factor between ALPGEN+PYTHIA MC09′ and ALPGEN+HERWIG/JIMMY AUET1 illustrate differences between PYTHIA and HERWIG/JIMMY and their interplay with the matrix-element/parton-shower matching implemented in ALPGEN. Differences between the different ALPGEN+PYTHIA tunes illustrate the large impact of the underlying-event and parton-shower tune on the leading-order prediction of the cross section. In particular, the difference in the value of the normalization is largest for the ALPGEN+PYTHIA D6 tune, which is the only PYTHIA tune that uses Q^2-ordering in the parton showering. It has been hypothesized that the different parton shower models available in PYTHIA and HERWIG may, through the MLM-matching used in ALPGEN, have a significant effect on the overall prediction of the cross section. This issue would benefit from additional studies, and perhaps dedicated tuning of ALPGEN+PYTHIA or ALPGEN+HERWIG.

The most fundamental result in the multi-jet analysis is the cross section as a function of the inclusive jet multiplicity. Figure 7 shows the results for the selected data sample. The measurement systematics are dominated by the jet energy scale uncertainty and go from 10-20% at low multiplicities to almost 30-40% at high multiplicities. This is primarily due to the increasing steepness of the differential cross section as a function of the n^{th} jet for increasing n. The Monte Carlo simulation predictions fall on the measured results across the full inclusive multiplicity spectrum. The normalization applied to the ALPGEN samples is closer to unity than for the PYTHIA samples, except for the ALPGEN+PYTHIA MC09′ and D6 samples.

A study that reduces significantly the impact of systematic uncertainties is the ratio of the n-jet cross section to $(n-1)$-jet cross section as a function of multiplicity. In this ratio, the impact of the jet energy scale uncertainty is significantly reduced and the uncertainty due to the luminosity cancels out. Figure 8 shows the results for such a study. Both the unfolding and the jet energy scale uncertainties contribute comparably to the total systematic uncertainty, and the statistical uncertainties are smaller than the systematic uncertainties, and negligible in most bins. The ALPGEN+HERWIG AUET1 prediction represents the data well within the error bands, and so do the other Monte Carlo simulations. The

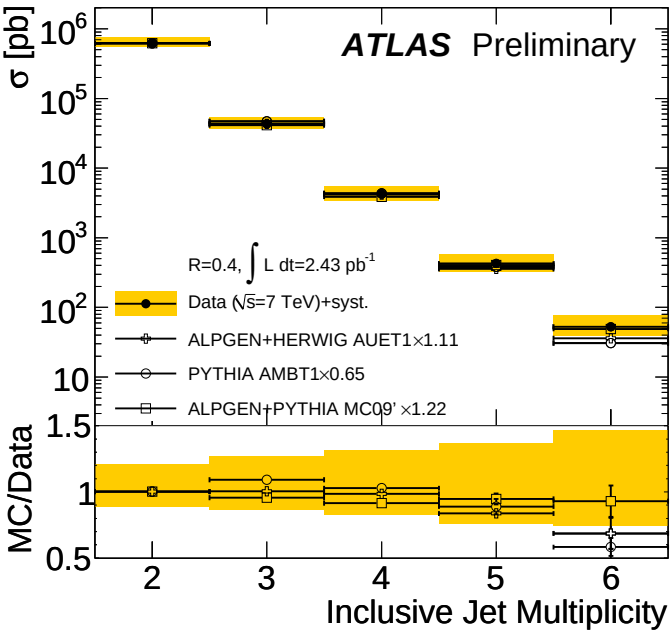

Figure 7: Total inclusive jet cross section as a function of multiplicity. The data are compared to leading-order Monte Carlo simulations (ALPGEN+HERWIG AUET1, ALPGEN+PYTHIA MC09′ and PYTHIA AMBT1) normalized to the measured two-jet inclusive jet multiplicity bin. The orange error bands correspond to the systematic uncertainties. A plot of the ratio of the different Monte Carlo simulations to the data is presented at the bottom of the figure.

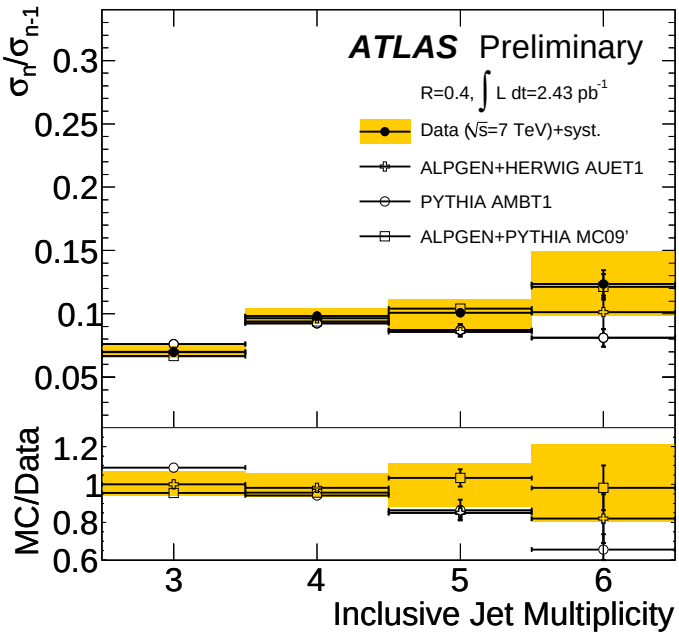

Figure 8: Ratio of the n-jet cross section to the $(n-1)$ jet cross section for values of n varying from three to six. Systematic uncertainties on the cross sections are included as an error band. The results are compared to leading-order parton-shower Monte Carlo simulations. The error bands correspond to the uncertainties as in Figure 7. A plot of the ratio of the different Monte Carlo simulations to the data is presented at the bottom of the figure.

PYTHIA AMBT1 Monte Carlo simulation predicts a somewhat higher (lower) three-to-two jet (four-to-three jet) cross-section ratio, implying that it does not match the shape of the inclusive distribution as well as the different ALPGEN predictions. Differences at the level of 15% are observed between PYTHIA AMBT1 and ALPGEN+PYTHIA MC09′ in the first bin. These differences could arise not only from the difference between the ME+PS and the pure parton-shower Monte Carlo simulations, but also the different pdfs used in PYTHIA AMBT1 and ALPGEN+PYTHIA MC09′. All ALPGEN+PYTHIA tunes studied follow each other closely in this measurement, despite the different normalizations shown in Table 3.

The differential cross section for multi-jet events as a function of p_{T} provides probably one of the most informative results that can be used to estimate jet backgrounds in searches beyond the Standard Model. These events represent a major QCD background and by tagging the momentum dependence, one can hone in on searches over various mass ranges. This study also validates shapes that affect the unfolded jet inclusive cross section measurement. Figure 9 presents the p_{T} dependent differential cross sections for the leading, second leading, third leading and fourth leading jet for multi-jet events. The systematic uncertainty in the measurement is 10-20% across p_{T} and increasing up to 30% for the 4^{th} leading jet differential cross section. The jet energy scale systematic uncertainty remains the dominant uncertainty in the measurement. The ALPGEN+HERWIG AUET1 and ALPGEN+PYTHIA MC09′ Monte Carlo simulations are in agreement with the data within the systematic uncertainties. The two Monte Carlo simulations follow each other closely. The shape of the other ALPGEN+PYTHIA Monte Carlo simulations is similar to that of the ALPGEN tunes shown, except for the D6 tune, which follows the data even more closely. The shape of the PYTHIA AMBT1 is steeper than that of the data for Figures 9 (a) and (b), and a similar feature has been observed in the PYTHIA Perugia2010 prediction.

A similar study to the p_{T} dependent differential cross section is the differential cross section for multi-jet production as a function of H_{T}, namely the scalar sum of the p_{T} of selected jets in the event. As an example, the H_{T} distributions are particularly useful for top quark studies. Figure 10 gives the results for the H_{T} dependent differential cross sections compared to the ALPGEN and PYTHIA Monte Carlo simulations. Similar conclusions as those reached in the previous figure can be drawn.

One of the QCD studies that is most sensitive to limitations in the leading-order Monte Carlo simulations and next-to-leading-order calculation, due to the small systematic uncertainties on the measurement, is the ratio of the inclusive three to two jet differential cross section as a function of some characteristic scale of the event. Figure 11 presents the results for the measurement of the three-to-two jet cross-section ratio as a function of $p_{\mathrm{T}}^{\mathrm{lead}}$ for jets with $R = 0.4$ and $R = 0.6$, whereas Figure 12 presents the results for the same ratio as a function of $H_{\mathrm{T}}^{(2)} = p_{\mathrm{T}}^{\mathrm{lead}} + p_{\mathrm{T}}^{\mathrm{sec}}$, for jets with $R = 0.4$ and $R = 0.6$. These results are complementary to the next-to-leading-order analysis presented later in this section, and thus shown for two jet resolution parameters. The cross section ratio as a function of $p_{\mathrm{T}}^{\mathrm{lead}}$ is of interest, in particular, for the tuning of final state radiation. The ratio as a function of $H_{\mathrm{T}}^{(2)}$ is shown due to its stability under renormalization scale variations in the next-to-leading-order calculation, discussed at the end of this section.

The systematic uncertainties on both these measurements are small ($\approx$ 5%) and dominated by the systematic uncertainties in the unfolding correction. That systematic uncertainty is somewhat larger in the first bin due to the impact of the event selection cut on the shape of the leading jet p_{T} distribution for $N_{\mathrm{jets}} \geq 3$. Both ratios show similar features. The ALPGEN+HERWIG AUET1 continues to describe the data within systematic uncertainties. The shape descriptions from PYTHIA AMBT1 do not describe the data so well. At low p_{T} and $H_{\mathrm{T}}^{(2)}$, PYTHIA predicts a larger three-jet cross section than what is measured. The effect becomes even larger when PYTHIA Perugia2010 is used. All the ALPGEN+PYTHIA tunes studied show the opposite effect, even though it is smaller, and often within the systematic uncertainties in the measurement.

A comparison between Monte Carlo simulation and data is performed on the three angular distri-

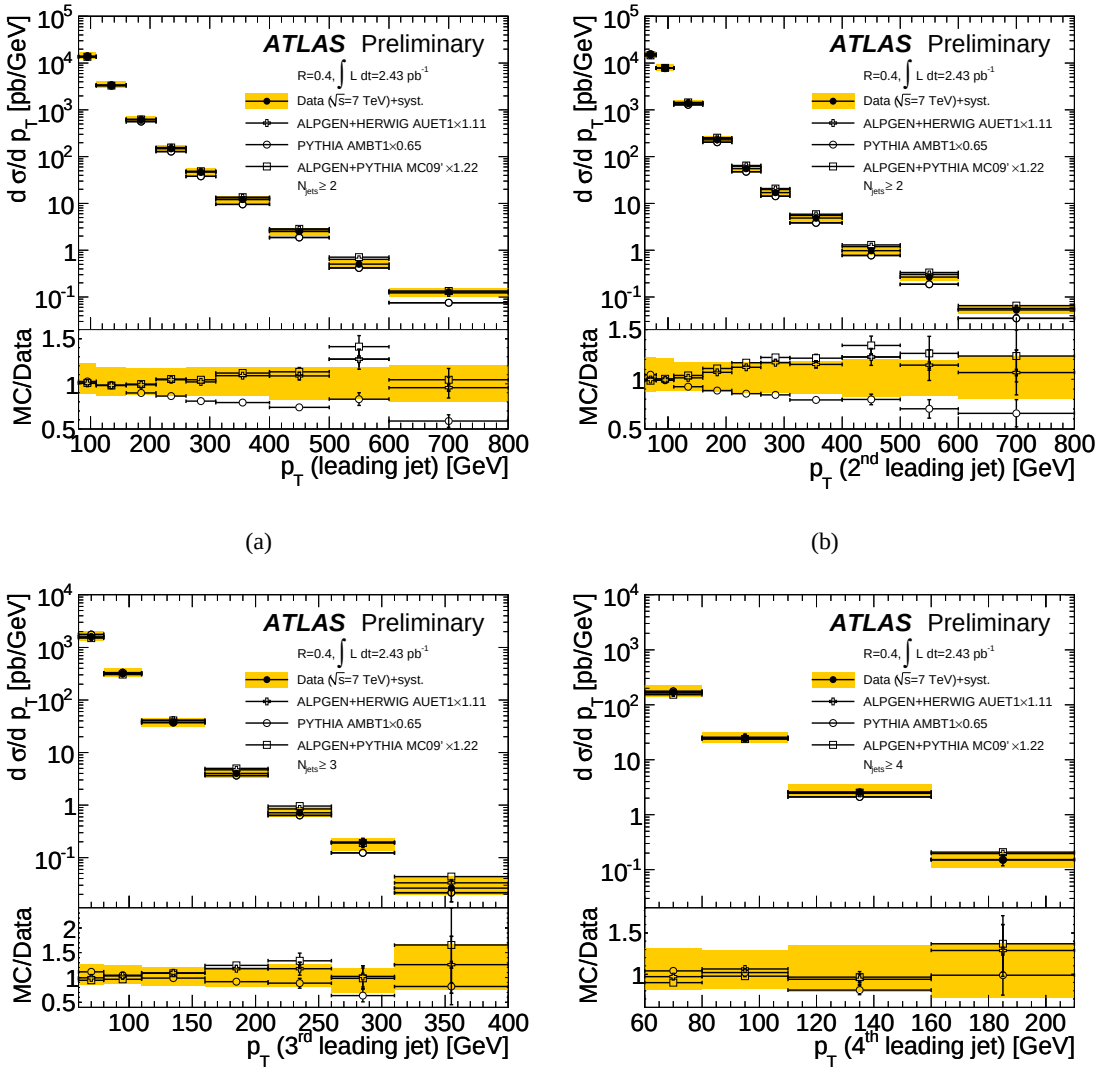

Figure 9: Differential cross section as a function of leading jet p_{T} for events with $N_{\mathrm{jets}} \geq 2$ (a), 2nd leading jet p_{T} for events with $N_{\mathrm{jets}} \geq 2$ (b), 3rd leading jet p_{T} for events with $N_{\mathrm{jets}} \geq 3$ (c) and 4th leading jet p_{T} for events with $N_{\mathrm{jets}} \geq 4$ (d). The results are compared to different leading-order Monte Carlo simulations normalized to the measured two-jet inclusive jet multiplicity bin. The error bands correspond to the uncertainties as in Figure 7. A plot of the ratio of the different Monte Carlo simulations to the data is presented at the bottom of the figure.

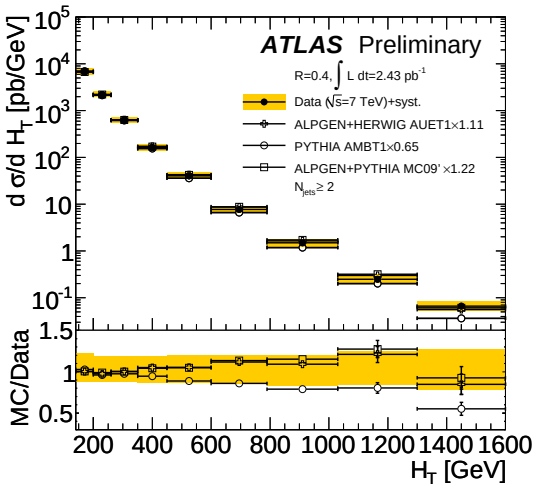

(a)

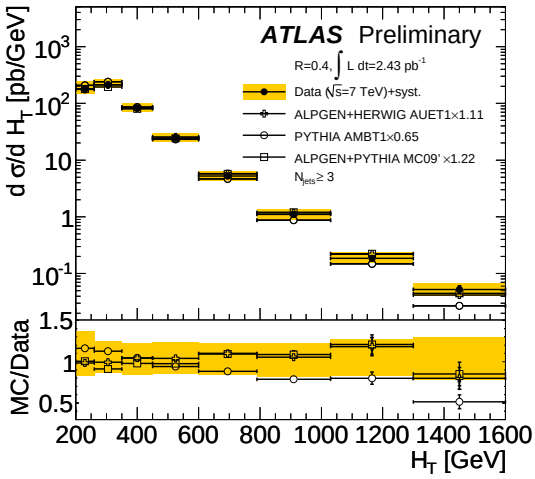

(b)

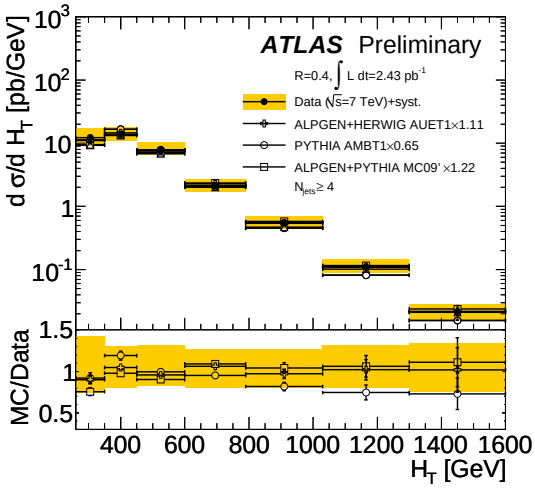

(c)

Figure 10: Differential cross section as a function of H_T for events with at least two selected jets (a), three selected jets (b) and four selected jets (c). The results are compared to different leading-order Monte Carlo simulations normalized to the measured two-jet inclusive jet multiplicity bin. The error bands correspond to the uncertainties as in Figure 7. A plot of the ratio of the different Monte Carlo simulations to the data is presented at the bottom of the figure.

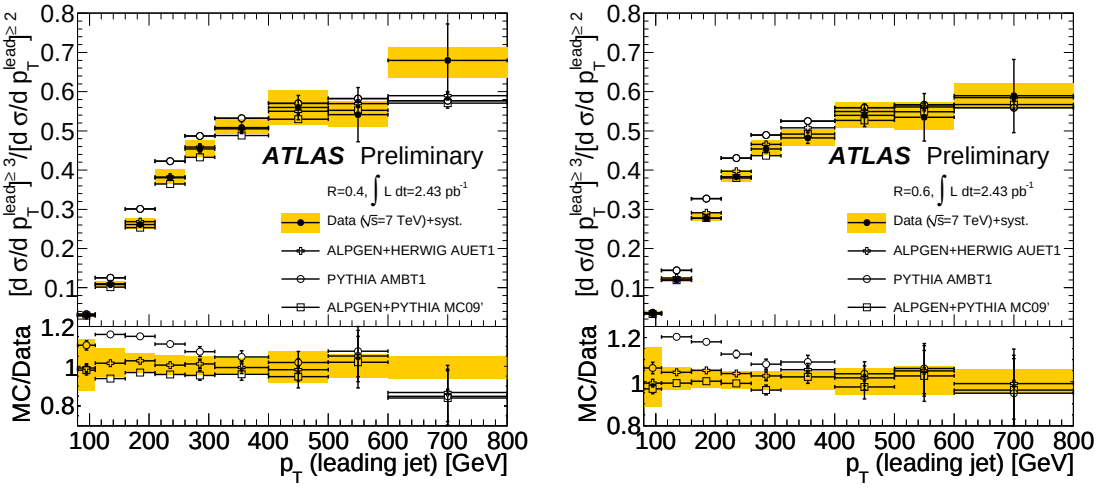

(a) (b)

Figure 11: Ratio of the three-to-two jet differential cross-section ratio as a function of the leading jet p_{T}. The left and right figures correspond to R = 0.4 and R = 0.6, respectively. The results are compared to leading-order parton-shower Monte Carlo simulations. The error bands correspond to the uncertainties as in Figure 7. A plot of the ratio of the different Monte Carlo simulations to the data is presented at the bottom of the figure.

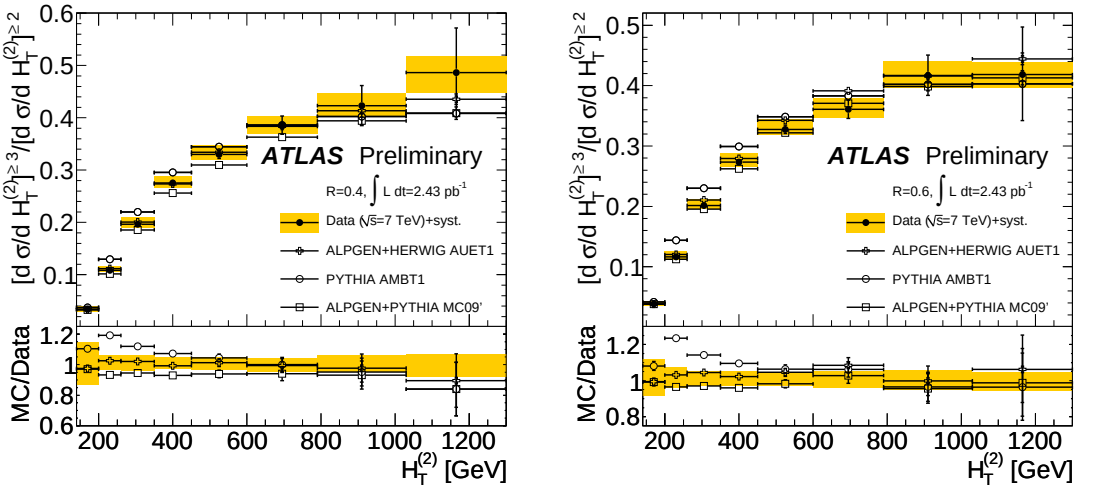

(a) (b)

Figure 12: Ratio of the three-to-two jet differential cross-section ratio as a function of the sum of the p_{T} of the two leading jets. The left and right figures correspond to R = 0.4 and R = 0.6, respectively. The results are compared to leading-order parton-shower Monte Carlo simulations. The error bands correspond to the uncertainties as in Figure 7. A plot of the ratio of the different Monte Carlo simulations to the data is presented at the bottom of the figure.

butions ($\Delta\phi$ as well as $\Delta\eta$) in events with three or more jets. The distributions are normalized by the inclusive three-jet cross section, since shape comparisons are most interesting in this context. Figure 13 shows the three $|\Delta\phi|$ results. A similar study for $|\Delta\eta|$ is shown in Figure 14.

Note that the limited range of $|\eta| < 2.8$ provides a maximum separation between jet pairs of 5.6. However, the $\Delta\eta$ ranges in Figure 14 are truncated earlier due to the extremely low Monte Carlo simulation statistics available at very large $\Delta\eta$. The figures showing the angular spread between the first and the third leading jet and the second and the third leading jet (b and c) are truncated at small values of the angular spread, where they are dominated by jets that are very close to each other and whose angular resolution is understood less precisely. The different Monte Carlo simulations have low statistics in the tails. The systematic uncertainties are largely dominated by uncertainties in the unfolding, particularly those arising from the limited Monte Carlo simulation statistics available. The ALPGEN and PYTHIA MCs provide a reasonably good description of all the three $\Delta\phi$ distributions. At large $\Delta\eta$ between the second and the third leading jet the PYTHIA AMBT1 does not succeed at describing the data well, predicting a much larger population of events. A similar result has been observed for PYTHIA Perugia2010, while all the ALPGEN Monte Carlo simulations behave similarly to the ones shown in the figures.

Overall, at leading order, the ALPGEN+HERWIG AUET1 Monte Carlo simulation appears to do the best job at describing the multi-jet data, even though all the other ALPGEN Monte Carlo simulations used show similar features. After normalization to the measured two-jet inclusive cross section, most ALPGEN Monte Carlo simulations used predict an inclusive multi-jet cross section similar to the measured cross section (except for the ALPGEN+PYTHIA D6 tune), while the PYTHIA Monte Carlo simulations require large scaling factors to describe the inclusive multiplicity spectrum.

Calculations of QCD cross sections at next-to-leading order have a lower theoretical uncertainty than leading-order calculations and allow performing a consistent treatment of theoretical uncertainties more easily. If the next-to-leading-order calculation is not interfaced to a parton-shower generator, the event kinematics must be constrained to occur in parameter space regions where the fixed-order calculation is well defined. Figure 15 shows a comparison of the same results as Figure 11, but now compared to the next-to-leading-order calculation corrected for non-perturbative effects. Figure 16 shows a comparison of the same results as Figure 12, now again compared to the next-to-leading-order calculation corrected for non-perturbative effects.

The MSTW 2008 nlo pdf set has been used for the calculation shown in the figures, but comparable results are obtained with the CTEQ 6.6 pdf set. The systematic uncertainties on the theoretical prediction are shown as dotted red lines above and below the theoretical prediction. Good agreement is found between the data and the theory prediction within systematic uncertainties for both studies except in the lowest point. Due to the kinematic cuts applied in the analysis, the next-to-leading-order calculation accounts only for the lowest-order contribution to the two-jet cross section in the region $H_T^{(2)} < 160$ GeV; as a result, this effective leading-order estimation is subject to large theoretical uncertainties arising from higher-order terms, which might be responsible for the observed discrepancy. The larger theoretical uncertainty from the narrower $R = 0.4$ is apparent and not surprising, due to terms that enter the next-to-leading-order calculation as the logarithm of R. The overall comparison of Figure 15 and Figure 16 shows a substantially lower theoretical uncertainty for the $H_{\mathrm{T}}^{(2)}$ next-to-leading-order prediction, which makes the measurement a stringent test of pQCD. Given the small measurement uncertainties, the comparison in Figure 16 may be useful to constrain parameters entering the next-to-leading-order calculation, such as pdfs or the value of the strong coupling constant, α_S.

9 Summary and Conclusion

A first dedicated study of multi-jet events has been performed using the ATLAS detector at a center-of-mass energy of 7 TeV with an integrated luminosity of 2.43 pb^{-1}. For events containing two or more

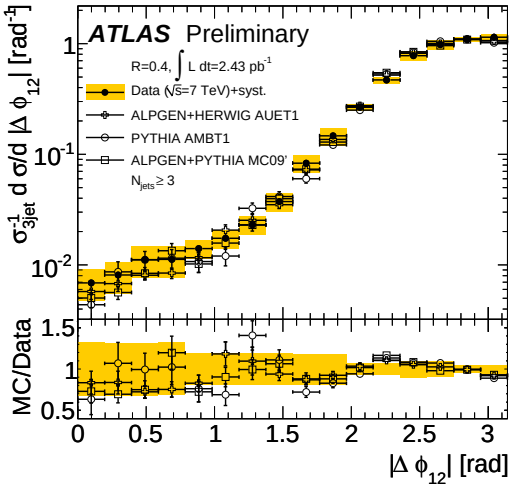

(a)

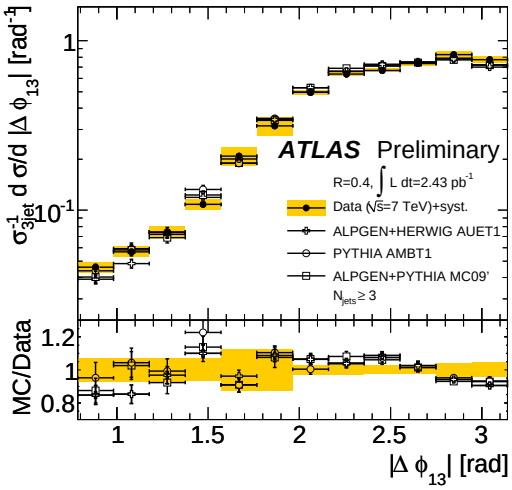

(b)

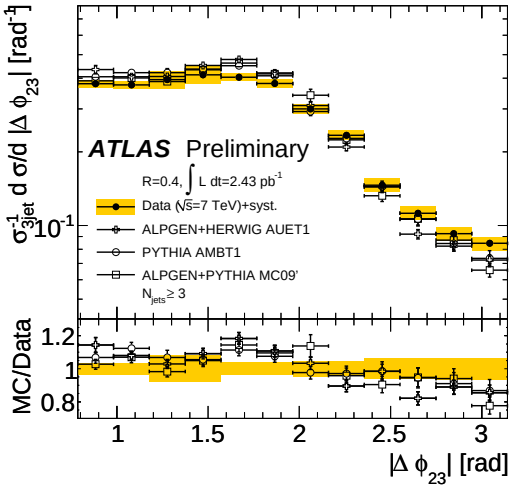

(c)

Figure 13: Differential cross section as a function of $\Delta\phi$ between (a) the leading and 2nd leading jet, (b) the leading and 3rd jet, (c) and the 2nd leading and 3rd leading jet for events with three or more jets in data (solid points) and leading-order Monte Carlo simulations (open markers). A plot of the ratio of the different Monte Carlo simulations to the data is presented at the bottom of the figure.

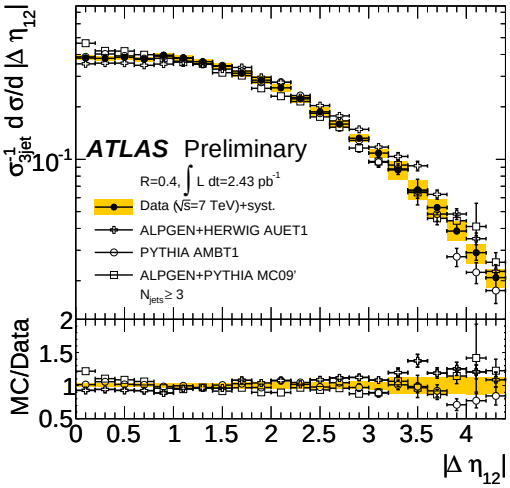

(a)

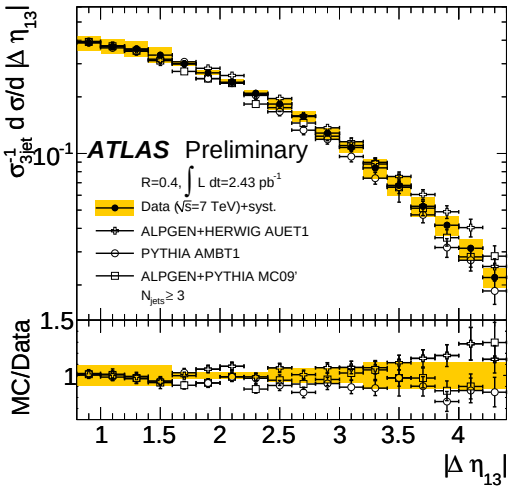

(b)

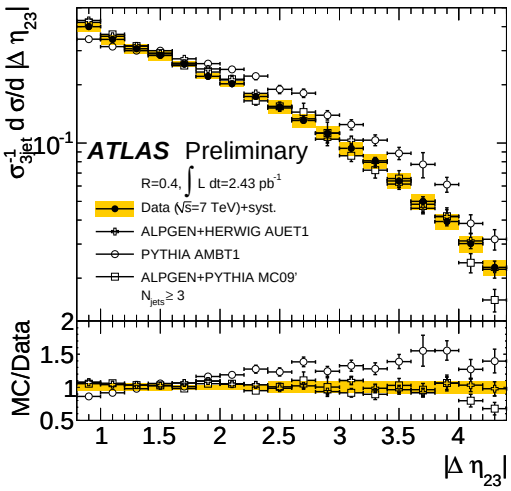

(c)

Figure 14: Differential cross section as a function of $\Delta\eta$ between (a) the leading and 2nd leading jet, (b) the leading and 3rd jet, (c) and the 2nd leading and 3rd leading jet for events with three or more jets in data (solid points) and leading-order Monte Carlo simulations (open markers). A plot of the ratio of the different Monte Carlo simulations to the data is presented at the bottom of the figure.

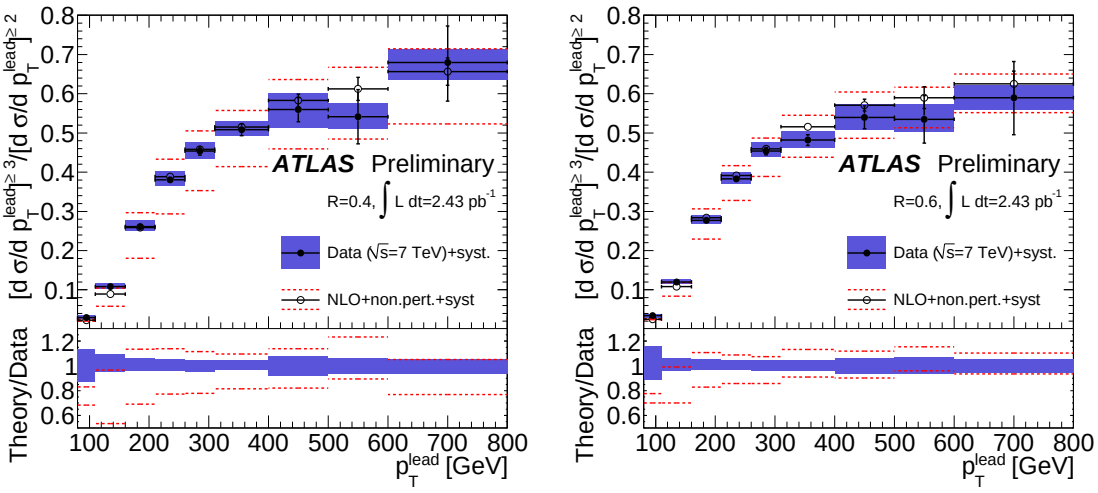

(a) (b)

Figure 15: Ratio of the three-to-two jet differential cross-section ratio as a function of the leading jet p_{T}. The left and right figures correspond to R = 0.4 and R = 0.6, respectively. The results are compared to next-to-leading-order pQCD calculations with the MSTW 2008 nlo pdf set. The data error bands are identical to the results shown in Figure 11. The systematic uncertainties on the theoretical prediction are shown as dotted red lines above and below the theoretical prediction. A plot of the ratio of the next-to-leading-order calculation to the data is presented in the figure beneath.

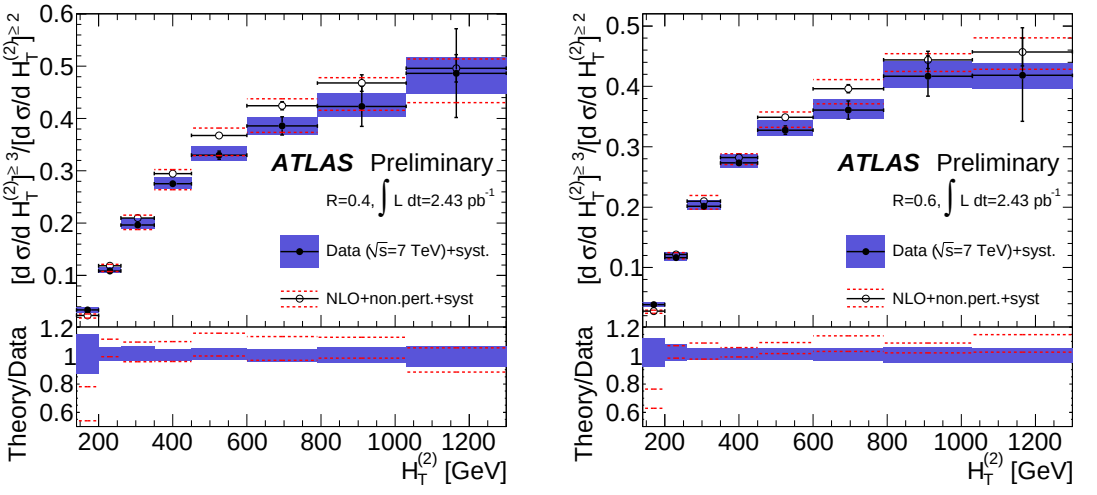

(a) (b)

Figure 16: Ratio of the three-to-two jet differential cross-section ratio as a function of the sum of the p_{T} of the two leading jets. The left and right figures correspond to R = 0.4 and R = 0.6, respectively. The results are compared to next-to-leading-order pQCD calculations with the MSTW 2008 nlo pdf set. The data error bands are identical to the results shown in Figure 12. The systematic uncertainties on the theoretical prediction are shown as dotted red lines above and below the theoretical prediction. A plot of the ratio of the next-to-leading-order calculation to the data is presented in the figure beneath.

jets with $p_{\mathrm{T}} \geq 60$ GeV, of which at least one has $p_{\mathrm{T}} \geq 80$ GeV, good agreement is found between data and leading-order Monte Carlo simulations with parton-shower tunes that describe adequately the ATLAS $\sqrt{s} = 7$ TeV underlying-event data. The agreement is found after the predictions of the Monte Carlo simulations are normalized to the measured inclusive two-jet cross section. The models have been compared to multi-jet inclusive and differential cross sections as well as three-jet angular distributions. The present study extends up to a multiplicity of six jets, up to jet p_{T} of 800 GeV and up to event H_{T} (scalar sum of the p_{T}s of selected jets) of 1.6 TeV.

PYTHIA, which contains a $2 \rightarrow 2$ leading-order matrix element augmented by parton showers, does not describe the shapes of some of the studied distributions. This is most noticeable in the three-to-two jet cross-section ratios and the distributions of $\Delta\eta$ between the second and third leading jets. ALPGEN, which contains higher multiplicity tree-level matrix elements matched to parton showers, generally describes the shapes well, whether the HERWIG or PYTHIA parton showers are used. A measurement of the three to two jet cross section ratio as a function of the leading jet and the sum of the two leading jet p_{T}s has also been performed and is described by both ALPGEN and a next-to-leading-order pQCD calculation, albeit with a significant discrepancy in the lowest p_{T} bin. Comparisons with next-to-leading-order calculations may be useful to constrain parameters entering the next-to-leading-order calculation, such as pdfs or the value of the strong coupling constant, α_S, given the small measurement uncertainties, which are comparable to the systematic uncertainties in the theoretical prediction.

References

[1] A. Moraes, C. Buttar, and I. Dawson, *Prediction for minimum bias and the underlying event at LHC energies*, European Physical Journal C **50** (2007) .

[2] The ATLAS Collaboration, *Measurements of multi-jet production cross-sections in proton-proton collisions at 7 TeV center-of-mass energy with the ATLAS detector*, ATLAS Note **ATLAS-CONF-2010-084** (2010) .

[3] The ATLAS Collaboration, *The ATLAS Experiment at the CERN Large Hadron Collider*, JINST **3** (2008) S08003.

[4] R. Achenbach et al., *The ATLAS Level-1 Calorimeter Trigger*, Journal of Instrumentation **3** (March, 2008) P03001.

[5] M. Cacciari, P. G. Salam, and G. Soyez, *The anti-kt jet clustering algorithm*, JHEP **04** (2008) 063.

[6] M. Cacciari, G. P. Salam, G. Soyez, http://fastjet.fr/.

[7] S. Frixione and G. Ridolfi, *Jet photoproduction at HERA*, Nucl. Phys. B507 (1997) .

[8] The ATLAS Collaboration, *Measurement of underlying event characteristics using charged particles in pp collisions at $\sqrt{s}$ = 900 GeV and 7 TeV with the ATLAS detector*, Physical Review D (2010) accepted for publication.

[9] M. L. Mangano et al., *ALPGEN, a generator for hard multiparton processes in hadronic collisions*, JHEP **07** (2003) 001.

[10] J. Pumplin et al., *New generation of parton distributions with uncertainties from global QCD analysis*, JHEP **07** (2002) 012.

[11] T. Sjostrand, S. Mrenna, and P. Skands, *A Brief Introduction to PYTHIA 8.1*, Comput. Phys. Commun. **178** (2008) 852.

[12] T. Sjostrand et al., *High-energy physics event generation with PYTHIA 6.1*, Comput. Phys. Commun. **135** (2001) 238.

[13] G. Corcella et al., *HERWIG 6.5: an event generator for Hadron Emission Reactions With Interfering Gluons (including supersymmetric processes)*, JHEP **01** (2001) 010.

[14] G. Corcella et al., *HERWIG 6.5 release note*, arXiv:hep-ph/0210213.

[15] J. M. Butterworth and J. R. Forshaw, *Photoproduction of multi - jet events at HERA: A Monte Carlo simulation*, J. Phys. **G19** (1993) 1657.

[16] J. M. Butterworth, J. R. Forshaw, and M. Seymour, *Multiparton interactions in photoproduction at HERA*, Z. Phys. **C72** (1996) 637.

[17] The ATLAS Collaboration, *ATLAS Monte Carlo Tunes for MC09*, ATLAS Note **ATLAS-PHYS-PUB-2010-002** (2010) .

[18] The ATLAS Collaboration, *First tuning of HERWIG/JIMMY to ATLAS data*, ATLAS Note **ATLAS-PHYS-PUB-2010-014** (2010) .

[19] The ATLAS Collaboration, *Charged particle multiplicities in pp interactions measured with the ATLAS detector at the LHC.*, Tech. Rep. CERN-PH-EP-2010-079, CERN, Geneva, Dec, 2010.

[20] P. Z. Skands, *Tuning Monte Carlo generators: The Perugia tunes*, Phys. Rev. D **82** (Oct, 2010) 074018.

[21] A. Sherstnev and R. Thorne, *Different PDF approximations useful for LO Monte Carlo generators*, arXiv:0807.2132 [hep-ph].

[22] A. D. Martin et al., *Parton distributions for the LHC*, Eur. Phys. J. **C63** (2009) 189.

[23] CTEQ Collaboration, H. L. Lai et al., *Global QCD analysis of parton structure of the nucleon: CTEQ5 parton distributions*, Eur. Phys. J. **C12** (2000) 375.

[24] The ATLAS Collaboration, *The ATLAS Simulation Infrastructure*, arXiv:1005.4568. Accepted by Eur. Phys. J. C.

[25] S. Agostinelli et al., *Geant simulation*, Nucl. Instr. and Meth. A **506** (2003) 250.

[26] Z. Nagy, *Next-to-Leading order calculation of three jet observables in hadron hadron collisions*, Physical Review D (2003) 094002.

[27] P. M. Nadolsky et al., *Implications of CTEQ global analysis for collider observables*, Physical Review D **78** (2008) 013004.

[28] A.D. Martin et al., *Parton distributions for the LHC*, European Journal of Physics C **63** (2000) 189.

[29] The ATLAS Collaboration, *Performance of the ATLAS trigger in the early* $\sqrt{s}$ *= 7 TeV Data*, ATLAS Note **ATLAS-CONF-2010-094** (2010) .

[30] The ATLAS Collaboration, *Characterization of Interaction-Point Beam Parameters Using the pp Event-Vertex Distribution Reconstructed in the ATLAS Detector at the LHC*, ATLAS Note **ATLAS-CONF-2010-027** (2010) .

[31] The ATLAS Collaboration, *Performance of primary vertex reconstruction in proton-proton collisions at* $\sqrt{s}$*=7 TeV*, ATLAS Note **ATLAS-CONF-2010-069** (2010) .

[32] The ATLAS Collaboration, *Properties of Jets and Inputs to Jet Reconstruction and Calibration with the ATLAS Detector Using Proton-Proton Collisions at* $\sqrt{s}$*=7 TeV*, ATLAS Note **ATLAS-CONF-2010-053** (2010) .

[33] The ATLAS Collaboration, *Measurement of the* $W \to l\,\nu$ *and* $Z/\gamma \to l\,l$ *production cross sections in proton-proton collisions at* $\sqrt{s}$ *= 7 TeV with the ATLAS detector*, JHEP **12** (2010) 60.

[34] The ATLAS Collaboration, *Jet energy resolution and reconstruction efficiencies from in-situ techniques with the ATLAS Detector Using Proton-Proton Collisions at a Center of Mass Energy* $\sqrt{s}$*=7 TeV*, ATLAS Note **ATLAS-CONF-2010-054** (2010) .

[35] The ATLAS Collaboration, *Final jet energy scale and its systematic uncertainty for jets produced in proton-proton collisions at* $\sqrt{s}$*=7 TeV and measured with the ATLAS detector for the 2010 dataset*, ATLAS Note **ATLAS-CONF-2011-032** (2011) .

[36] The ATLAS Collaboration, *Azimuthal decorrelation in dijet events at* $\sqrt{s}$ *= 7 TeV*, ATLAS Note **ATLAS-CONF-2010-080** (2010) .

[37] The ATLAS Collaboration, *In-situ jet energy scale and jet shape corrections for multiple interactions in the first ATLAS data at the LHC*, ATLAS Note **ATLAS-CONF-2011-030** (2011) .

[38] The ATLAS Collaboration, *Updated Luminosity Determination in pp Collisions at* $\sqrt{s}$ *= 7 TeV using the ATLAS Detector*, ATLAS Note **ATLAS-CONF-2011-011** (2011) .